Open access • Journal Article • DOI:10.3847/1538-4357/AA603B

Cosmic-Ray Transport in Heliospheric Magnetic Structures. II. Modeling Particle Transport through Corotating Interaction Regions — Source link

A. Kopp, A. Kopp, T. Wiengarten, Horst Fichtner ...+5 more authors

Institutions: Université libre de Bruxelles, North-West University, Ruhr University Bochum, Stanford University ...+1 more institutions

Published on: 01 Mar 2017 - The Astrophysical Journal (IOP)

Topics: Heliosphere, Magnetohydrodynamics, Solar wind and Cosmic ray

The Astrophysical Journal, 837:37 (9pp), 2017 March 1 https://doi.org/10.3847/1538-4357/aa603b

Cosmic-Ray Transport in Heliospheric Magnetic Structures. II. Modeling Particle Transport through Corotating Interaction Regions

Andreas Kopp[1,2,6], Tobias Wiengarten[3], Horst Fichtner[3], Frederic Effenberger[4], Patrick Kühl[5], Bernd Heber[5], Jan-Louis Raath[2], and Marius S. Potgieter[2]

[1] Université Libre de Bruxelles, Service de Physique Statistique et des Plasmas, CP 231, B-1050 Brussels, Belgium
[2] Centre for Space Research, North-West University, 2520 Potchefstroom, South Africa
[3] Institut für Theoretische Physik IV, Ruhr-Universität Bochum, D-44780 Bochum, Germany
[4] Department of Physics and KIPAC, Stanford University, Stanford, CA 94305, USA
[5] Institut für Experimentelle und Angewandte Physik, Christian-Albrecht-Universität zu Kiel, D-24098 Kiel, Germany
Received 2016 November 25; revised 2017 February 3; accepted 2017 February 10; published 2017 March 1

Abstract

The transport of cosmic rays (CRs) in the heliosphere is determined by the properties of the solar wind plasma. The heliospheric plasma environment has been probed by spacecraft for decades and provides a unique opportunity for testing transport theories. Of particular interest for the three-dimensional (3D) heliospheric CR transport are structures such as corotating interaction regions (CIRs), which, due to the enhancement of the magnetic field strength and magnetic fluctuations within and due to the associated shocks as well as stream interfaces, do influence the CR diffusion and drift. In a three-fold series of papers, we investigate these effects by modeling inner-heliospheric solar wind conditions with the numerical magnetohydrodynamic (MHD) framework CRONOS (Wiengarten et al., referred as Paper I), and the results serve as input to a transport code employing a stochastic differential equation approach (this paper). While, in Paper I, we presented results from 3D simulations with CRONOS, the MHD output is now taken as an input to the CR transport modeling. We discuss the diffusion and drift behavior of Galactic cosmic rays using the example of different theories, and study the effects of CIRs on these transport processes. In particular, we point out the wide range of possible particle fluxes at a given point in space resulting from these different theories. The restriction of this variety by fitting the numerical results to spacecraft data will be the subject of the third paper of this series.

Key words: astroparticle physics – magnetohydrodynamics (MHD) – methods: numerical – solar wind – Sun: heliosphere

1. Introduction

As pointed out in the first paper of this series (Wiengarten et al. 2014, hereinafter Paper I), the understanding and appropriate modeling of the transport of energetic charged particles in turbulent magnetic fields remains one of the long-standing challenges in astrophysics and space physics. Despite the progress achieved during recent years (for recent reviews, see, e.g., Giacalone 2013; Schlickeiser 2015; Snodin et al. 2016), the corresponding theories have not yet matured into a coherent, (self-)consistent, and generally accepted state. This is, on the one hand, because the dependence of major transport processes, such as spatial and momentum diffusion as well as drifts in the large-scale magnetic field, on various parameters has not been clarified. On the other hand, the nature and properties of the turbulence is for most astrophysical systems not known in sufficient detail or even not known at all. Since the heliosphere offers the opportunity to measure the turbulent plasma that defines the transport environment of cosmic rays (CRs), it continues to be of unique significance as a natural laboratory for testing corresponding theories.

As is also pointed out in Paper I, to exploit this natural laboratory in full, it is necessary to reproduce all relevant measurements with simulations that do contain as much as possible of the three-dimensional structure of the plasma background within which the CRs are propagating. This is a task of magnetohydrodynamic (MHD) models that should eventually describe both the large-scale structure of the solar wind (see the brief review in Paper I) and its small-scale turbulent nature (see, e.g., Usmanov et al. 2011; Adhikari et al. 2015), desirably in a self-consistent way (Wiengarten et al. 2015, 2016; Usmanov et al. 2016). Of particular interest beyond the quiet, essentially latitudinally structured solar wind during the Sun's activity minima, characterized by the periodic heliospheric current sheet (HCS), are the (quasi-periodic) corotating interaction regions (CIRs), which form as a result of the interaction of fast with slow solar wind streams and usually persist for several solar rotations (see, e.g., Balogh et al. 1999, and references therein). As recently argued by Guo & Florinski (2014) and Guo & Florinski (2016), various questions are still unanswered, such as that of the modulation efficiency of CIRs on short timescales (e.g., Heber et al. 1999). By indirectly simulating neutron monitor data, Guo & Florinski (2014) found that CIRs—though occasionally referred to as "modulation barriers" (e.g., Toptygin 1985)—did actually facilitate the access of Galactic CRs (GCRs) significantly during the activity minimum of the solar cycle 23/24: the inclusion of CIRs into the modeling increased the GCR intensities by about 10%. In the improvement of this modeling, Guo & Florinski (2016) added a solar wind turbulence model and repeated the analysis. Differing from the first study, they found the HCS to have very little effect on short-term modulation, i.e., that variations in diffusion coefficients that can be related to stream interfaces inside CIRs are more important for GCR propagation than drift effects of the HCS, at least during a "negative" solar minimum, where positively

[6] Previously at the Institut für Experimentelle und Angewandte Physik, Christian-Albrecht-Universität zu Kiel, Germany.

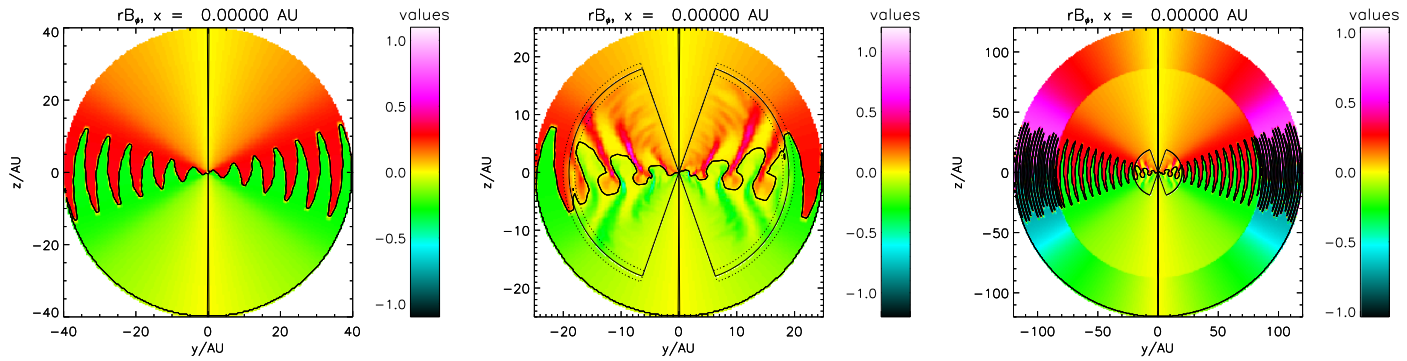

Figure 1. HMF visualized with its distance-weighted azimuthal component in the meridional y–z-plane, resulting from the analytical Parker spiral combined with the HCS (solid line) according to Equation (4) (left panel) and from a CRONOS simulation (middle panel) for a period when a CIR is present. The CRONOS configuration is computed within the area bounded by the solid lines and fitted to the analytical solution within the transition region indicated by the dotted lines. While these two panels show only an excerpt close to the Sun to visualize the coupling, the right panel shows the entire computational domain. As the outermost layer an inner heliosheath between the termination shock and the heliopause is modeled by letting the plasma flow and the HMF undergo a compression by a factor of 2.5 at the shock.

charged particles drift sunward along the HCS and then toward the poles.

In order to corroborate their findings, the study presented here improves that by Guo & Florinski (2014, 2016) in several respects. We employ the solar wind model computed with the CRONOS MHD framework in Paper I. In that model, first, the inner boundary is not at 0.5 au or 0.3 au but at 0.1 au, where oberservational input deriving from solar magnetograms can more realistically be employed via potential field modeling for the innermost region of the solar wind expansion. Consequently, the CIRs form naturally as a consequence of these input data and do not have to be introduced by an "artificially" prescribed modification of the inner boundary conditions. Second, we did not introduce a "virtual spacecraft" but demonstrated that with this model the in-ecliptic 1 au data from, e.g., the *STEREO A* and *B* spacecraft can be simulated satisfactorily. Third, in Paper I, we extended previous MHD simulations by simultaneously fitting in- and out-of ecliptic measurements. The latter were recorded by the *Ulysses* spacecraft and were also reproduced satisfactorily. Therefore, they were chosen as the basis for the CR transport simulations discussed below.

The paper is organized as follows. In Section 2, we describe the coupled MHD-CR transport model, the implemented diffusion and drift coefficients, as well as the boundary conditions. After a validation of the transport code, that is, employing the solution of the Parker equation by means of stochastic differential equations (SDEs), in Section 4, the results of simulations of a periodic three-dimensional (3D) and of a fully 3D, CIR-structured solar wind are presented and discussed. Following a brief summary of the main results, conclusions are drawn in the final section.

2. The Coupled MHD-CR Transport Model

In the following, we briefly describe the MHD model and summarize the findings of Wiengarten et al. (2013) and Paper I for the simulations of a periodic and a fully 3D-structured solar wind. Subsequently, we discuss the modeling of the CR transport based on SDEs and the coupling of the MHD results to it.

2.1. The MHD Model for the Solar Wind Background

2.1.1. The MHD Framework CRONOS

CRONOS is a fully MPI-parallel MHD code based on approximate Riemann solvers and is of second order in space and time. The solenoidality of the magnetic field is guaranteed by employing the constrained transport scheme. While, in general, Cartesian, cylindrical, and spherical polar coordinates are supported, the latter were chosen for the simulations discussed here. Further technical and alogrithmic details can be found in Appendix C in Wiengarten et al. (2015).

2.1.2. The Solar Wind Simulations

CRONOS simulations with 2D symmetry were presented in Wiengarten et al. (2013), where the model implementation was validated with comparisons to the analytical models by Parker (1958) and Weber & Davis (1967). For the 3D simulations as in Paper I, the innermost region of the solar wind acceleration is computed with a potential field model (solved with the "Finite Difference Iterative Poisson Solver" developed by Tóth et al. 2011). This allows us to use observed magnetograms recorded by the Global Oscillation Network Group (GONG, Harvey et al. 1996) as input to the Wang–Sheeley–Arge (WSA) model (Arge & Pizzo 2000; Arge et al. 2003) to compute the inner boundary conditions at a heliocentric distance of 0.1 au for our MHD simulations. With this setup, we computed in Paper I various 3D CIR-associated structures such as compression and rarefaction regions as well as forward and reverse shock pairs, all resulting "realistically" from the observed magnetic structure on the solar surface.

In a direct comparison of the simulation results with data from the *STEREO A* and *B* and the *Ulysses* spacecraft for the Carrington Rotations 2059, 2060, and 2061 in the year 2007, we have then demonstrated the capability of CRONOS to reproduce simultaneous multi-spacecraft observations including out-of-ecliptic data and considering temporally adjacent CIRs. In order to provide a suitable input to the CR transport model of the present paper these simulations of Paper I now extend to an outer boundary of 20 au and cover the Carrington Rotations 2057–2062. While these results are shown along with the solutions of the CR transport equation in the following sections, Figure 1 (middle panel) exemplarily illustrates a

typical solution for the strength of the heliospheric magnetic field (HMF) that is 3D structured due to the presence of a CIR. The still existing limitations regarding memory and disk space requested in the radial direction to either increase the size of grid cells or to limit the radial extension of the computational area. The scale factors lead to a decrease of the time-step the closer the boundary approaches the poles. In order to obtain a solution within a sufficiently fine grid resolution that converges with a reasonable time, the CRONOS solution had to be limited to 15 au in the radial direction and between 23° and 157° in the latitudinal direction (see Figure 3). This region fully covers the selected part of the *Ulysses* trajectory considered below, so that this spatial limitation of the numerical MHD solution does not affect the results of the present study.

An outer boundary at 15 au, however, has consequences for modeling the CR transport. In particular, it is necessary to first propagate the Local Interstellar Spectrum (LIS) at the heliopause (see the right panel in Figure 1) inward and then to provide the resulting CR spectrum as a boundary condition for particles leaving the heliosphere. Aside from the technical realization, an artificially close boundary leads to an incorrect solution of the transport equation as demonstrated for the case of Jovian electrons by Vogt et al. (2015). In the present study we thus treaded another path, visualized by zooming into the simulation region in the left and middle panels of Figure 1: the distance of the outer boundary and the LIS are kept at the quantities given below. Instead, an analytical Parker solution with a wavy HCS (left panel) is adapted in the azimuthal direction and concerning the tilt angle (see below) to the CRONOS solution (within the solid lines in the middle panel). The two solutions are then fitted by linear interpolation within a transition region of ±5 au (dotted lines). The entire simulation used for the particle transport is shown in the right panel of Figure 1. A comparison between this approximation of the background field close to the poles and a test scenario, where particles reaching the boundary in the latitudinal direction are treated as being lost, revealed that their contribution to the results can be neglected. The only limitation left is the fact that CIRs beyond 15 au cannot be taken into account.

2.2. The CR Transport Model

While there is general agreement that the quantitative treatment of the CR transport in the heliosphere should be based on the Parker equation (Parker 1965), there is considerable disagreement as to the spatial and energy dependence of the elements of the diffusion tensor κ and the particle drift velocity $\langle \boldsymbol{v}_{\rm d} \rangle$. Therefore, after a brief description of the explicit form of the transport equation and the method of SDEs, we present different diffusion tensors and drift velocity representations, which are used for the simulations of the CR transport.

2.2.1. Transport Equation and Method of Solution

Parker's transport equation for the distribution function f, which is a function of space $\boldsymbol{r}$ (in spherical polar coordinates with radius r, co-latitude ϑ, and azimuth φ), rigidity P and time t reads

$$\frac{\partial f}{\partial t} = -(\boldsymbol{v}_{\rm sw} + \langle \boldsymbol{v}_d \rangle) \cdot \nabla f + \nabla \cdot (\kappa \cdot \nabla f) + \frac{1}{3}(\nabla \cdot \boldsymbol{v}_{\rm sw}) \frac{\partial f}{\partial \ln P} + S, \quad (1)$$

describing convection, diffusion, and adiabatic losses of the CR particles. In addition to the quantities introduced above, $\boldsymbol{v}_{\rm sw}$ denotes the solar wind velocity, and S is a particle source such as Jovian electrons.

Instead of applying traditional finite-difference methods, the transport Equation (1) is solved by the method of SDEs (e.g., Zhang 1999), where phase-space elements, so-called pseudo-particles, are propagated through the phase-space and binned subsequently. The numerical code is based on Kopp et al. (2012), where details about the method and its numerical realization can also be found. Equation (1) has to be transferred to a system of Langevin-type equations, which can be found, e.g., in Strauss et al. (2012) or Raath et al. (2015, 2016) and consist each of a deterministic convective part and a stochastic diffusive part.

2.2.2. The Transport Coefficients

In this study, we apply the transport model for GCR protons in the heliosphere by Potgieter et al. (2014) with slightly modified parameters (see Raath et al. 2015, 2016).

The analytic configuration has a Parker HMF

$$\boldsymbol{B}_0 = \frac{a_0}{r^2}[\boldsymbol{e}_r - \Gamma(r, \vartheta)\boldsymbol{e}_\varphi] \quad (2)$$

with $\Gamma(r, \vartheta) = (\Omega_\odot r \sin\vartheta)/v_{\rm sw}$. Here, $\Omega_\odot$ is the solar angular velocity, and the factor a_0 is determined by values at the Earth orbit: $a_0 = B_{\rm Earth}/\sqrt{1 + \Gamma\left(1\ {\rm au}, \frac{\pi}{2}\right)^2}$.

This field changes its sign at the wavy HCS:

$$\boldsymbol{B} = \boldsymbol{B}_0(1 - 2\Theta(\vartheta - \vartheta_{\rm HCS})), \quad (3)$$

where Θ is the Heaviside function. The latitudinal extension of the HCS is determined by the tilt angle α. As a function of azimuth, the co-latitude of the HCS is

$$\vartheta_{\rm HCS}(r, \varphi) = \frac{\pi}{2} - \arctan(\sin\varphi^* \tan\alpha) \quad (4)$$

with $\varphi^* = \varphi + \varphi_0 + \Gamma\left(r, \frac{\pi}{2}\right)$. For a discussion of alternative formulations, see Raath et al. (2015). The constant φ_0 and the tilt angle α were determined by fitting the analytical configuration to the CRONOS output.

The solar wind velocity is purely radial with 400 km s^{-1} in the equatorial region and increases sharply at $\vartheta = \frac{\pi}{2} \pm \vartheta_{\rm T}$ (with $\vartheta_{\rm T} = \alpha + 15° \frac{\pi}{180°}$) toward the poles to 800 km s^{-1}. At the termination shock, the velocity decreases by a factor of 0.4.

In a local system with the z-direction along the magnetic field, the diffusion tensor is diagonal with the components $\kappa_{\perp,r}$, $\kappa_{\perp,\vartheta}$, and $\kappa_\parallel$. The parallel diffusion coefficient is the same as that in Potgieter et al. (2014):

$$\kappa_\parallel = \kappa_{\parallel,0}\beta K(P)\left(\frac{B_0}{B}\right). \quad (5)$$

Here, β is the ratio of the particle speed and the speed of light, $\kappa_{\parallel,0}$ is a constant, and K is a function of rigidity (see Potgieter et al. 2014). The two perpendicular components are

$$\kappa_{\perp,r} = 0.02\kappa_\parallel$$
$$\kappa_{\perp,\vartheta} = 0.02\tilde{f}_\vartheta(\vartheta)\kappa_\parallel, \quad (6)$$

where $\tilde{f}_\vartheta$ is the function in Equation (8) of Potgieter et al. (2014; the anisotropic case) or $\tilde{f}_\vartheta = 1$ (the isotropic case).

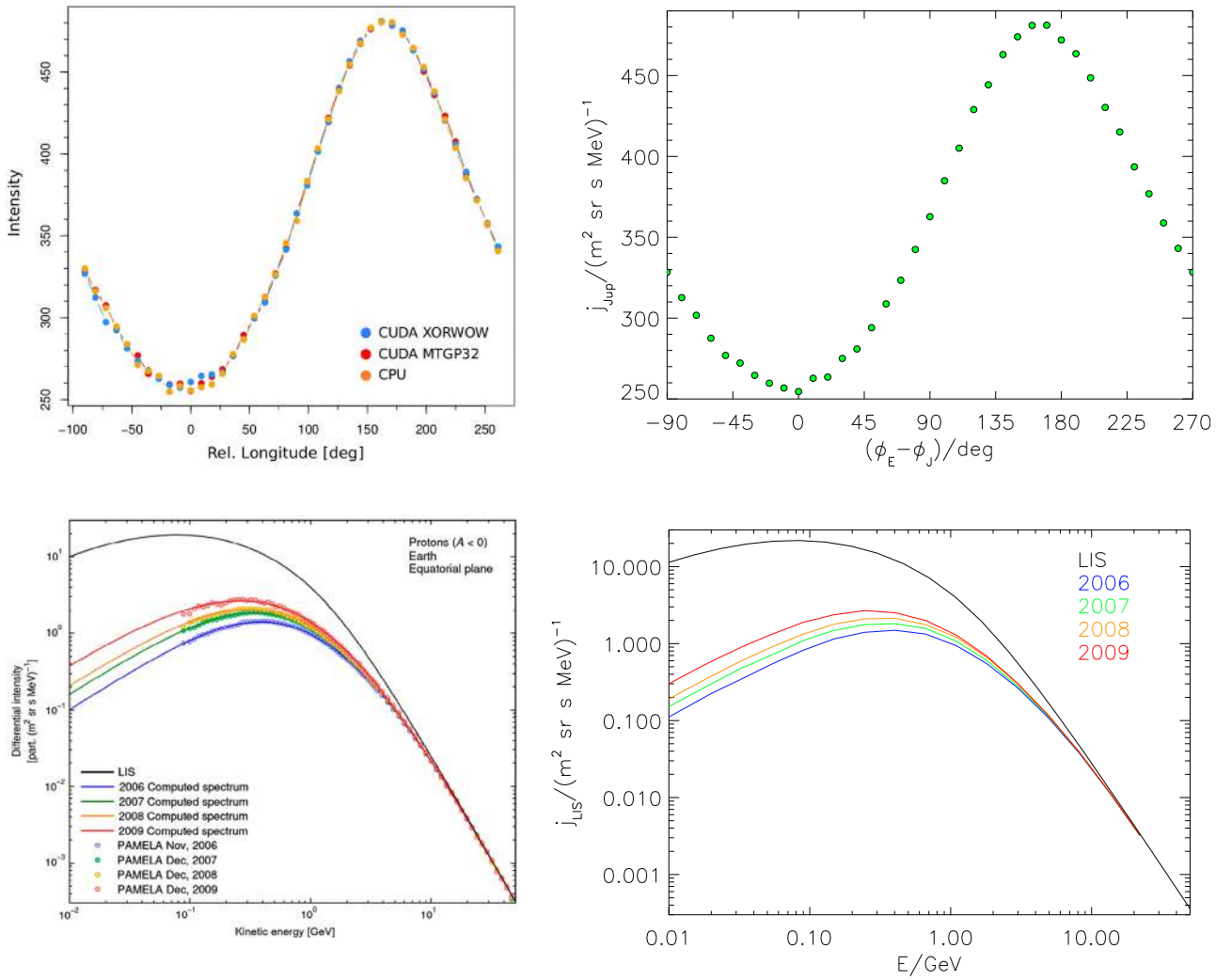

Figure 2. Upper panels: azimuthal variation of Jovian electrons at the Earth' orbit computed by Dunzlaff et al. (2015), who implemented SDEs on graphics processing units (GPUs, left), and by the present implementation (right). Lower panels: modulated GCR proton spectra at Earth for the years 2006–2009 during an $A < 0$-drift cycle computed with the finite-differences code by Potgieter et al. (2014, left) and the SDE approach described here (right). The data in the lower left panel indicate measurements made with the *PAMELA* spacecraft.

There are three possibilities to transform this local tensor into the global system: (1) according to Burger et al. (2008) for the case $B_\vartheta = 0$, (2) same, but for the general case, and (3) with a local trihedron according to Effenberger et al. (2012). For a Parker field and $\tilde{f}_\vartheta = 1$ all three representations lead to the same diffusion tensor. For case (3), $\kappa_{\perp,\vartheta}$ no longer has the meaning of a "ϑ component" of the diffusion tensor, so that subsequently only the isotropic case is taken into account.

For the drifts, we use (e.g., Jokipii et al. 1977)

$$\langle \boldsymbol{v}_{\rm d} \rangle = \nabla \times \left(\frac{P\beta}{3B^2} \boldsymbol{B} \right). \tag{7}$$

While this expression can be evaluated analytically even for modifications to the Parker field (see Raath et al. 2016), there are mainly two possibilities to numerically realize the current sheet drift (to treat the jump in Equation (3)): use the magnetic field given by Equation (3) or apply the algorithm by Strauss et al. (2012) to determine the distance L of the pseudo-particles to the HCS and compute the drift according to Equations (17) and (18) of Strauss et al. (2012). This possibility is called "Strauss1" (st1) in the following. Version "Strauss2" (st2) is essentially the same, but uses the angles defined by Burger (2012) and takes into account the r-dependency of the solar wind (see, e.g., Raath 2015).

The second possibility is to smooth out the HCS (Burger 2012) and to compute the drift contributions analytically as given in Equation (13) of Burger (2012). Version "Burger1" (bg1) omits the last contribution of this equation, while "Burger2" (bg2) uses the full equation.

The two Strauss versions differ only marginally, while "Burger2" (case not shown) features lower intensities and an asymmetry between the two hemispheres not being present in the other cases, possibly requiring an adaption of the model parameters to the SDE approach (R. A. Burger, 2014 private communication), so that we restrict ourselves here to cases "st2" and "bg1." "nd" notes the case, where no drift effects at all were taken into account.

For the simulations shown subsequently, the TS is located at 86 au (Potgieter et al. 2014, for the year 2007), the heliopause at 120 au (see the right panel of Figure 1). The tilt angle is fitted to $\alpha = 21°$ and deviates from $\alpha = 14°$ given by Potgieter et al. (2014). The boundary conditions in the two angular directions are the same as in Strauss et al. (2011). At the inner boundary, we employ reflecting boundary conditions ($\partial f/\partial t = 0$). The

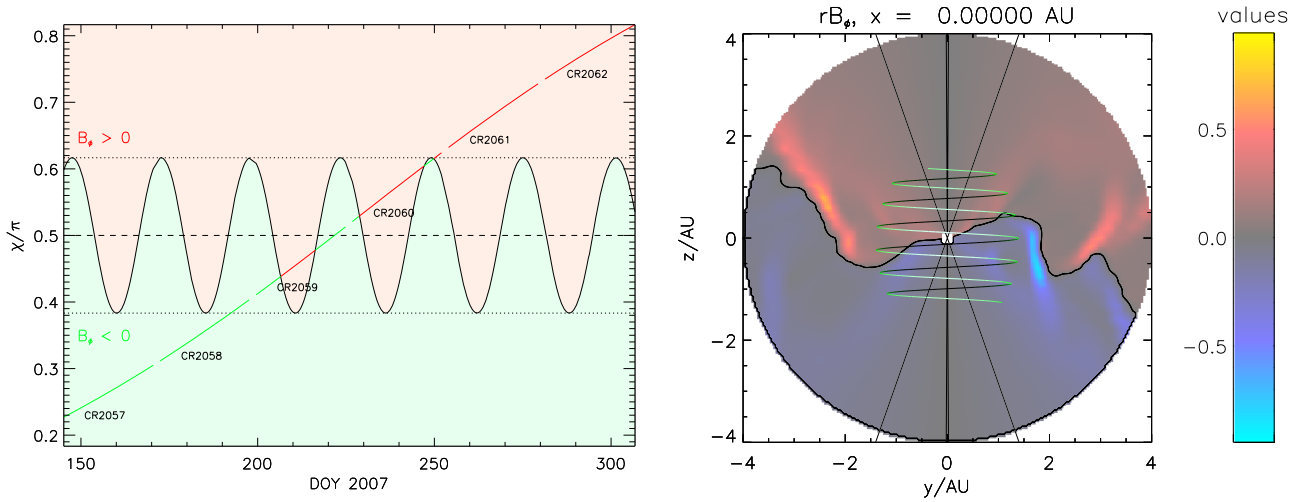

Figure 3. Trajectory of the *Ulysses* spacecraft in the considered time period, i.e., the Carrington Rotations 2057–2062 in the year 2007. The left panel shows the variation in co-latitude χ superimposed onto the HCS with areas of positive and negative B_φ shown in red and green, respectively. The dashed line is the equatorial plane, the two dotted lines indicate the extension of the HCS. The right panel is a projection of the trajectory onto the meridional y–z-plane in a system corotating with the Sun, where the spacecraft moves from south to north. The background coloring indicates the distance-weighted azimuthal component (rB_φ) of the HMF. In both panels, the wavy solid black line is the HCS.

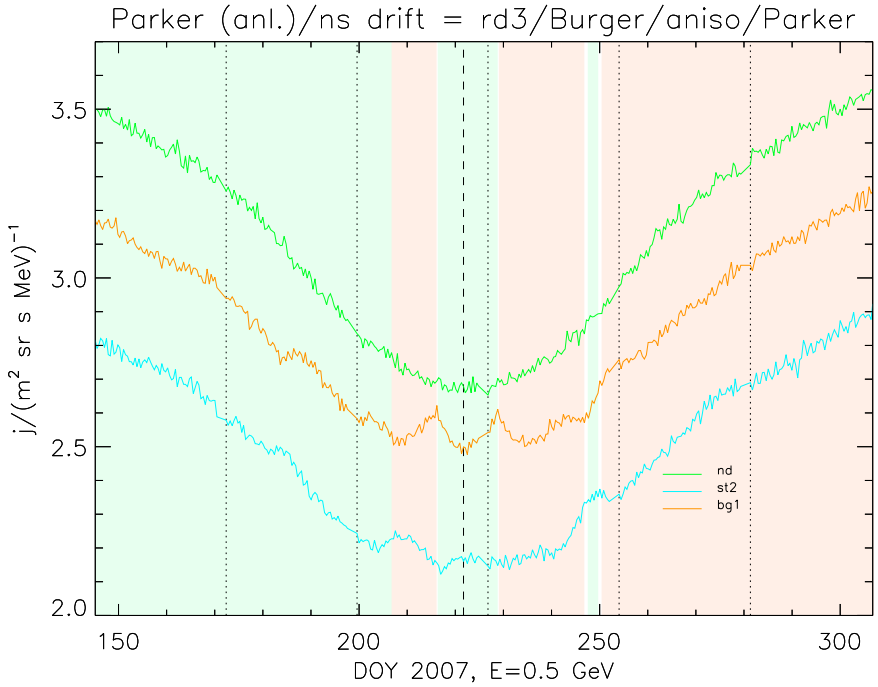

Figure 4. Intensity of 500 MeV GCR protons along the *Ulysses* trajectory in 2007 in the analytical Parker HMF solution with a tilt angle of $\alpha = 21°$ as a function of time. The colored lines stand for a reduced (rd3) selection of formulations of the drift: no drifts (green), "Burger1" (orange), and "Strauss2" (blue). The green, white, and red shading indicate positions of *Ulysses* above, within and below the HCS, respectively. The dashed vertical line shows the equatorial plane, the dotted lines separate the individual Carrington Rotations.

outer boundary is, apart from the validation case below, the LIS by Webber & Higbie (2003) because we compare the results only among each other, but not with data. For a comparison with data (which we intend to do in the third paper) we will have to start with finding a more realistic LIS. The coupling of the two codes will be described in Section 4.

3. Code Validation

In order to validate the new numerical code, we compared our results with those of two earlier applications: the propagation of Jovian electrons studied by Dunzlaff et al. (2015) and the GCR proton spectra obtained by Potgieter et al. (2014). For the first case, the upper panels of Figure 2 show the flux of Jovian electrons as a function of the relative azimuthal angle φ (with respect to that of Jupiter) obtained by Dunzlaff et al. (2015, left panel) and by the present study (right panel). For the second case, the lower panels compare proton spectra for the $A < 0$ cycle during the years 2006–2009 by Potgieter et al. (2014; left panel) with those obtained with the new code (right panel). The LIS used here is a slightly modified version of that given by Potgieter et al. (2014). Note that the spectra by Potgieter et al. (2014) were

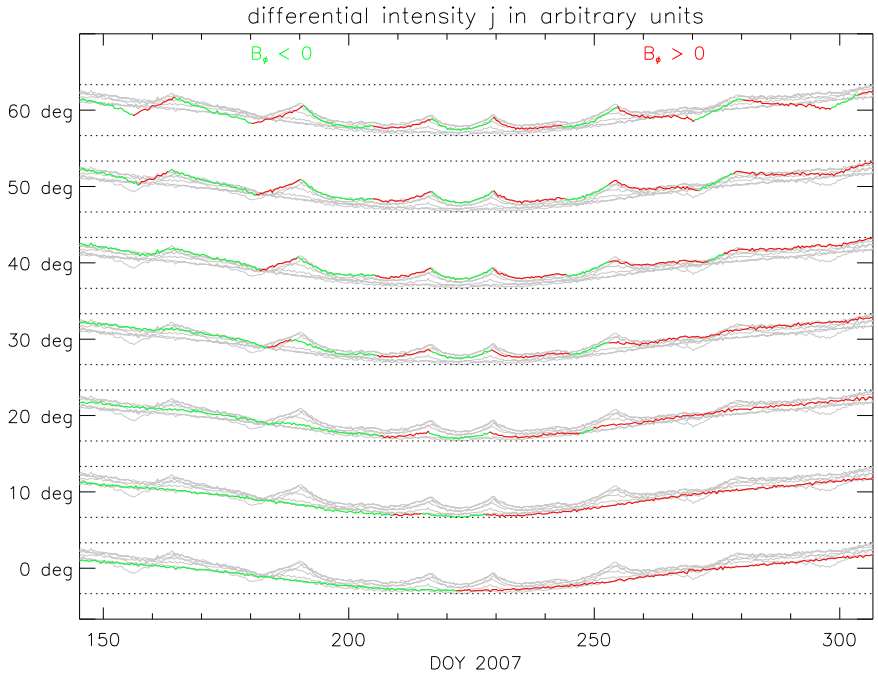

Figure 5. Intensity of 500 MeV GCR protons along the *Ulysses* trajectory in 2007 in an analytical Parker spiral magnetic field for different tilt angles of the HCS, from $\alpha = 60°$ (top panel) to $\alpha = 0°$ (bottom panel). The gray lines show the intensities for all tilt angles (in order to compare the amplitudes), the colored ones show that for the respective tilt angle with red and green for positive (above the HCS) and negative (below the HCS) values of B_φ, respectively.

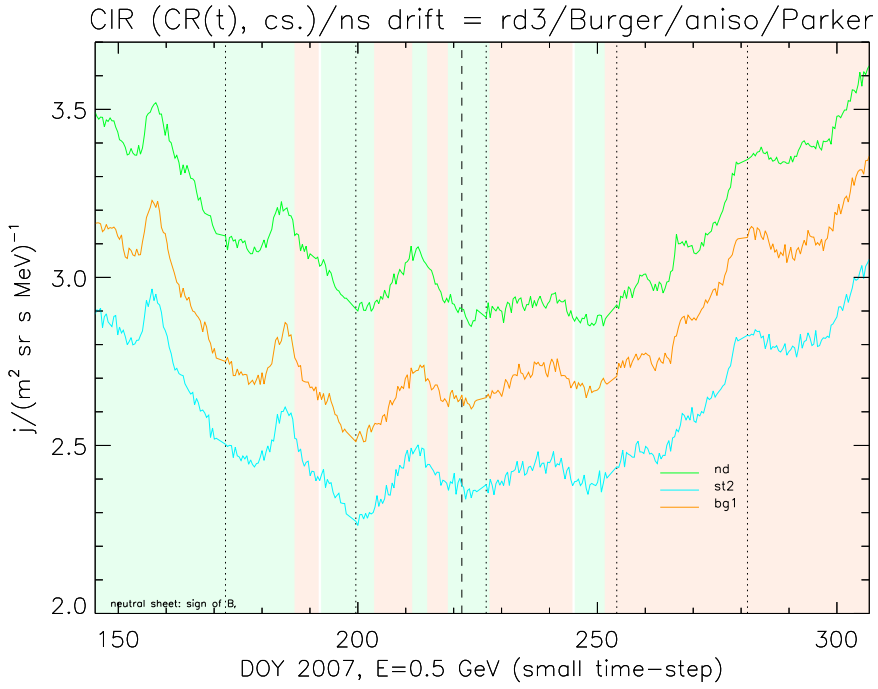

Figure 6. Same as Figure 4 but for the full 3D numerical solution with CIRs.

obtained by a finite-difference code, so that slightly different transport parameters had to be used (see Raath 2015; Raath et al. 2016). In both cases, we evidently obtain very good agreement between the old and new simulations, so we may consider the new numerical framework as validated.

4. Simulation Results

For the simulations, we have selected the period of the Carrington Rotations 2057–2062, i.e., 2007 May to November. This is a so-called $A < 0$ drift cycle, i.e., positively charged particles drift sunward along the HCS, which was tilted by on average 21°, and then toward the poles. This value derived by fitting the CRONOS and Parker solutions is consistent with that obtained from the Wilcox Solar Observatory (WSO) modeling (see, e.g., http://wso.stanford.edu/Tilts.html). This selection enables a comparison with data recorded by the *Ulysses* spacecraft that went, following its third south polar path, from about −40° to +55° in heliocentric latitude

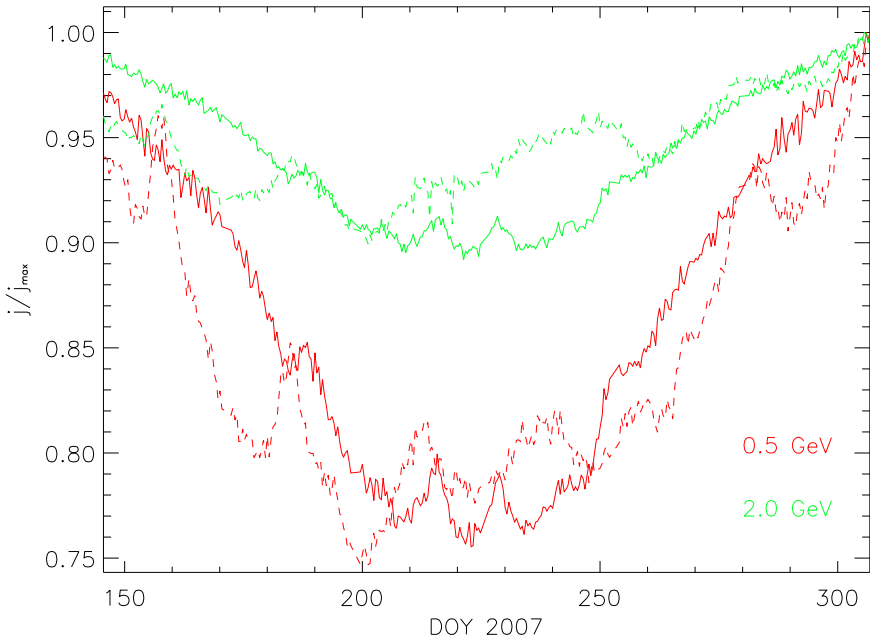

Figure 7. Intensity of 500 MeV (red) and 2 GeV (blue) GCR protons along the *Ulysses* trajectory (see Figure 6) for the "Burger1" drift, normalized to the respective maximum. The solid and dashed lines stand for the periodic 3D analytical and fully 3D numerical solution with CIRs, respectively.

and between 1.39 and 1.67 au in heliocentric distance (see Figure 3).

The fact that this period is also covered in the studies by Guo & Florinski (2014) and Guo & Florinski (2016) allows a partial comparison with their findings. In the following subsections, we present and discuss the simulation results for the CR proton transport in two heliospheric configurations, namely in a periodic (the variation in the azimuthal direction is determined merely by the HCS) 3D-structured solar wind without CIRs and in a fully 3D, CIR-structured solar wind.

We simulated each Carrington Rotation individually and read the CRONOS output of velocity and magnetic field (in hdf5 format) for all Carrington Rotations into the transport code. The transport quantities were computed as functions of the local velocity and magnetic field on the CRONOS grid. The configuration for each point of the *Ulysses* trajcectory was interpolated linearly in time between the CRONOS output for the Carrington Rotation belonging to the respective point and that of the closest neighbor (Carrington Rotation ± 1, see the Appendix) and subsequently treated as "frozen," i.e., fixed in time. During the propagation, the transport quantities for the pseudo-particles along their (phase-space) trajectories were interpolated linearly in space onto the CRONOS grid. An interpolation also in time for each point along the entire trajectory for each pseudo-particle is already implemented, but its realization is, however, currently beyond the possibilities regarding storage and performance time.

4.1. Transport in a 3D Periodically Structured Solar Wind

First, we study, as a reference case, a heliospheric configuration without CIRs but with the effect of a wavy HCS. The latter is assumed to be tilted by 21° as explained above. In this configuration, the waviness of the HCS is exclusively affecting the direction (sign) of the HMF, i.e., not the velocity field of the solar wind. Consequently, the latter is only two-dimensionally structured in heliographic latitude. The same applies to the spatial diffusion tensor that is not sensitive to the sign of the HMF. So, merely the particle drifts do respond to the HCS's waviness. In difference to at least the parallel diffusion coefficient, Equation (5), for which the quasilinear result is generally accepted (see, e.g., Fichtner 2005; Florinski et al. 2013), for the current sheet drifts no specific representation has, as yet, been agreed on. Therefore, we considered the two drift models described above and the no-drift case. The corresponding three simulations result in the differential intensity of 500 MeV GCR protons along the *Ulysses* trajectory and are shown in Figure 4.

The overall shape of the curves is the same, namely a nearly north–south symmetric increase of intensity with increasing heliographic latitude as a consequence of the large-scale diffusion of the particles. The figure further shows that the no-drift (nd) case yields higher intensities than the drift cases in an $A < 0$ solar activity cycle for the chosen tilt angle and the radial distance of the *Ulysses* trajectory. This result is consistent, e.g., with the findings by Webber et al. (1990; see also Strauss et al. 2012 or Raath 2015). The significance of the drift effect is emphasized by the differences between the two different cases: first, their overall intensity differences are of the same order as that of the "Burger1" (bg1) drift to the no-drift case. Second, HCS crossings appear to be more pronounced for the "Burger1" drift case than for the "Strauss2" (st2) drift, which is a consequence of the different treatment (including the choice of parameters) of the HCS drift. Such details should eventually allow one to determine which is the more appropriate one.

It is well-known that the differential intensity at a given heliospheric position depends on the tilt angle of the HCS sheet (see also Raath et al. 2015). In order to illustrate this effect, Figure 5 shows the results for seven different tilt angles for the "Burger1" drift. Again as expected, the intensity curves along the *Ulysses* trajectory exhibit more structure with increasing tilt angle. This is naturally explained by the accordingly increasing number of HCS crossings (indicated in the figure by the change of the line color from red to green and vice versa). Note that in view of the uncertainty in the determination of the tilt angle (see, e.g., http://wso.stanford.edu/Tilts.html) the results for up to 30°–40° are actually relevant for the interpretation of data

recorded during the selected time period, while those for higher values merely serve to illustrate the effect, but might be relevant for other periods of time.

4.2. Transport in a fully 3D, CIR-structured Solar Wind

After having established a reference case with the simulations described in the previous subsection, we can now turn to the full 3D case with which we attempt to simulate the proton intensities along the *Ulysses* trajectory more realistically. For this purpose, we use as a crucial input for the solar wind modeling the GONG maps for the selected six Carrington Rotations. As demonstrated in detail in Paper I, this allows a suitable, realistic simulation of the 3D-structured solar wind. The main difference to the reference case (periodic 3D) is the presence of CIRs, which evolve naturally from the complex input in the form of the GONG maps for each Carrington Rotation. This is illustrated with the middle panel in Figure 1 for Carrington Rotation 2060.

The differential intensities of Galactic protons at 500 MeV for this scenario are plotted in Figure 6, which is the analogue to Figure 4. The diffusion tensor here and in all numerical solutions shown below was computed according to Burger et al. (2008) for general B_{ϑ} (case (2) above) and isotropic perpendicular diffusion. All findings that were read off the latter figure also hold for this more realistic case, i.e., the overall shape of the curves remains dominated by the large-scale diffusion, and the no-drift case has the highest intensity, while the "Strauss2" drift case has the lowest. There are, however, two significant differences. First, the use of the actual magnetic field structure at the inner boundary introduces quasi-periodic CIR patterns. This is most pronouncedly seen in the first four of the six considered Carrington Rotations, where four intensity peaks mark the presence of CIRs. These increased intensities reflect a temporary "trapping" of GCR protons inside CIRs due to the increased turbulence and, thus, decreased diffusion therein. Second, the amplitude of the intensity variation is smaller than in the case without CIRs: while the maximum values at the beginning and the end of the considered time period (when *Ulysses* was located at higher heliographic latitudes) are about the same in both cases (see the left panel of Figure 7), the minimum levels around day 222 in Figures 4 and 6 (when *Ulysses* was close to the ecliptic) are significantly (about 10%) higher when CIRs are present. On the one hand, this finding of reduced modulation of GCR protons in the presence of CIRs confirms the analogous result arrived at by Guo & Florinski (2014), who employed a similar, albeit simplified, simulation and nearly the same diffusion setup. On the other hand, here the simulations are extended to higher latitudes, where this effect of the CIRs is, as one should expect, much weaker and even reversed (see below).

The new model can, of course, be used to study the GCR proton intensity at different energies. Figure 7 gives, exemplarily, the result for 500 MeV and 2 GeV for both the periodic and full 3D cases. Evidently, the overall change in differential intensity with latitude is smallest for the highest energy. This direct comparison of the 3D CIR case (dashed lines) with the no-CIR case (solid lines) reveals that the effect of the CIRs is basically the same at these energies, but also that the increase of intensity as compared to the no-CIR case is limited to low heliographic latitudes and does not simply vanish toward high latitudes but reverses at mid-latitudes, where the presence of CIRs appears to increase the modulation energy-dependently. It is to be expected that the details of this intensity behavior depend on the chosen diffusion model. While we have employed here a diffusion tensor that is consistent with that used by Guo & Florinski (2014), future parameter studies should be performed with improved turbulence models, such as the one-component model incorporated by Guo & Florinski (2016) or the two-component model (Oughton et al. 2011) that was recently extended to 3D and self-consistency (Wiengarten et al. 2016).

5. Summary and Conclusions

In this second paper in a series of three, we have combined a cosmic-ray transport model with the MHD model presented in Paper I. As described in the latter, this model enables simulations using actual magnetic maps provided by the GONG collaboration and suitably derived plasma conditions as inner boundary conditions and, thus, allows one to describe the 3D-structured and time-varying solar wind in comparatively realistic detail. Consequently, employing an SDE approach, we were able to simulate the GCR proton transport in a complex, realistically space- and time-varying solar wind flow with a self-consistently computed magnetic field.

We demonstrated the capability of the extended simulation model by applying it to the Carrington Rotations 2057–2062 in the year 2007, which coincide with the so-called third fast latitude scan of the *Ulysses* spacecraft. With various simulations, we studied, as a reference case, a periodically 3D-structured solar wind and compared it to the more realistic full 3D case that, as a consequence of the use of the observed magnetic field as an inner boundary condition, is highly structured and, in particular, leads to the formation of CIRs. This way we extended earlier work that was limited to both the use of idealized boundary conditions not related to actual measurements and to low latitudes close to the ecliptic plane.

We confirmed that CIRs decrease the modulation in the ecliptic, but found that this effect reverses at mid-latitudes before it almost vanishes at high latitudes, where, consistently, the effect of CIRs should be minimal. While this effect of CIRs is present for both energies considered (0.5 and 2 GeV), its amount diminishes with increasing energy.

Finally, we illustrated the still existing considerable uncertainty of such simulations, particularly with regard to the drift model, for which no general agreement has been achieved as yet, but also regarding the (time-interpolation) of the MHD background field structure of the diffusion tensor, the diffusion model or the proper choice of the LIS.

Besides the comparison with spacecraft data (to be done in the third paper of the series) in order to narrow the range of "allowed" CR transport parameters, future extensions of the work should comprise an incorporation of state-of-the-art turbulence transport models.

We would like to thank the referee for helpful comments. Financial support via projects FI 706/14-1 and HE 3279/15-1 funded by the Deutsche Forschungsgemeinschaft (DFG) is acknowledged. The work was partly carried out within the framework of the bilateral BMBF-NRF-project "Astrohel" (01DG15009) funded by the Bundesministerium für Bildung und Forschung. M.S.P. and J.L.R. acknowledge the partial financial support of the South African Research Foundation (NRF) under the German-South African Research Cooperation Programme, grant UID 93132.

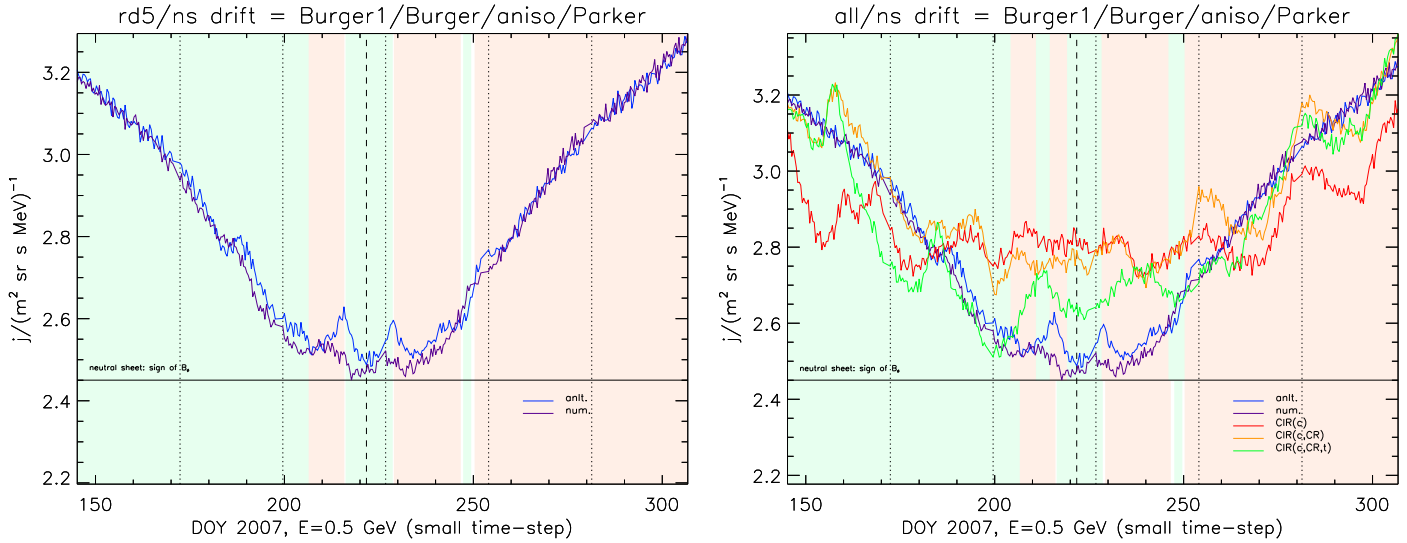

Figure 8. Differential intensities for the case shown in Figures 4 (periodic 3D analytic) and 6 (full 3D numerical), but for the "Burger1" drift alone and for different numerical realizations: Parker analytical (blue), Parker numerical (violet), and the three CRONOS configurations explained in the text. The blue and green curves are identical to the orange curves in Figures 4 and 6, respectively. The left panel shows only the two Parker cases with the shading for the HCS from Figure 4, the right one shows all cases (with the HCS—upper part—as in Figure 6). The lower part (below the solid black line) of the shading shows, in both panels, the Parker HCS.

Appendix
Numerical Tests

As explained in Section 4, we compared the transport of GCRs in an analytically computed Parker configuration with that in a numerical configuration computed by the CRONOS code. As a first test, we compare the analytical solution with "free" functions of space (which are used throughout this study) and with interpolations onto the CRONOS grid. These two cases are shown in the left panel of Figure 8 by the blue and violet curves, respectively. The differential intensities coincide within the statistical fluctuations for large parts of the trajcetory, but differ when *Ulysses* crosses the HCS (background color changes from green to red or vice versa). The analytical curves (blue) are more pronounced due to the finer resolution of the drift (again "Burger1"). The right panel shows, in addition, three cases computed with the CRONOS code (note the different background shading in the upper part, which now corresponds to the green curve). The first case (red) uses Carrington Rotation 2060 for the entire trajectory, the second one (orange) uses the respective Carrington Rotation, and the third one (green) interpolates between using the (preceding or subsequent) Carrington Rotation. Carrington Rotation 2060 can be easily identified as that where the red and orange curves coincide (within the statistical fluctuations), while the green curve crosses the orange one in the central parts of each Carrington Rotation.

References

Adhikari, L., Zank, G. P., Bruno, R., et al. 2015, ApJ, 805, 63
Arge, C. N., Odstrcil, D., Pizzo, V. J., & Mayer, L. R. 2003, in AIP Conf. Ser. 679, ed. M. Velli et al. (Melville, NY: AIP), 190
Arge, C. N., & Pizzo, V. J. 2000, JGR, 105, 10465
Balogh, A., Gosling, J. T., Jokipii, J. R., Kallenbach, R., & Kunow, H. 1999, SSRv, 89
Burger, R. A. 2012, ApJ, 760, 60
Burger, R. A., Krüger, T. P. J., Hitge, M., & Engelbrecht, N. E. 2008, ApJ, 674, 511
Dunzlaff, P., Strauss, R. D., & Potgieter, M. S. 2015, CoPhC, 192, 156
Effenberger, F., Fichtner, H., Scherer, K., et al. 2012, ApJ, 750, 108
Fichtner, H. 2005, AdSpR, 35, 512
Florinski, V., Ferreira, S. E. S., & Pogorelov, N. V. 2013, SSRv, 176, 147
Giacalone, J. 2013, SSRv, 176, 73
Guo, X., & Florinski, V. 2014, JGRA, 119, 2411
Guo, X., & Florinski, V. 2016, ApJ, 826, 65
Harvey, J. W., Hill, F., Hubbard, R. P., et al. 1996, Sci, 272, 1284
Heber, B., Sanderson, T. R., & Zhang, M. 1999, AdSpR, 23, 567
Jokipii, J. R., Levy, E. H., & Hubbard, W. B. 1977, ApJ, 213, 861
Kopp, A., Büsching, I., Strauss, R. D., & Potgieter, M. S. 2012, CoPhC, 183, 530
Oughton, S., Matthaeus, W. H., Smith, C. W., Breech, B., & Isenberg, P. A. 2011, JGR, 116, A08105
Parker, E. N. 1958, ApJ, 128, 664
Parker, E. N. 1965, P&SS, 13, 9
Potgieter, M. S., Vos, E. E., Boezio, M., et al. 2014, SoPh, 289, 391
Raath, J.-L. 2015, Master's thesis, Northwestern Univ.
Raath, J. L., Potgieter, M. S., Strauss, R. D., & Kopp, A. 2016, AdSpR, 57, 1965
Raath, J. L., Strauss, R. D., & Potgieter, M. S. 2015, Ap&SS, 360, 56
Schlickeiser, R. 2015, PhPl, 22, 091502
Snodin, A. P., Shukurov, A., Sarson, G. R., Bushby, P. J., & Rodrigues, L. F. S. 2016, MNRAS, 457, 3975
Strauss, R. D., Potgieter, M. S., Büsching, I., & Kopp, A. 2011, ApJ, 735, 83
Strauss, R. D., Potgieter, M. S., Büsching, I., & Kopp, A. 2012, Ap&SS, 339, 223
Toptygin, I. N. 1985, Cosmic Rays in Interplanetary Magnetic Fields, (Dordrecht: Reidel)
Tóth, G., van der Holst, B., & Huang, Z. 2011, ApJ, 732, 102
Usmanov, A. V., Goldstein, M. L., & Matthaeus, W. H. 2016, ApJ, 820, 17
Usmanov, A. V., Matthaeus, W. H., Breech, B. A., & Goldstein, M. L. 2011, ApJ, 727, 84
Vogt, A., Kühl, P., Heber, B., Kopp, A., & Dunzlaff, P. 2015, Proc. ICRC, 34, 207
Webber, W. R., & Higbie, P. R. 2003, JGRA, 108, 1355
Webber, W. R., Potgieter, M. S., & Burger, R. A. 1990, ApJ, 349, 634
Weber, E. J., & Davis, L., Jr. 1967, ApJ, 148, 217
Wiengarten, T., Fichtner, H., Kleimann, J., & Kissmann, R. 2015, ApJ, 805, 155
Wiengarten, T., Kleimann, J., Fichtner, H., et al. 2013, JGRA, 118, 29
Wiengarten, T., Kleimann, J., Fichtner, H., et al. 2014, ApJ, 788, 80
Wiengarten, T., Oughton, S., Engelbrecht, N., et al. 2016, ApJ, 833, 17
Zhang, M. 1999, ApJ, 513, 409